

High Thermal Conductivity of Sandwich-Structured Flexible Thermal Interface Materials

Lin Jing, Rui Cheng, Muzzafer Tasoglu, Zexiao Wang, Qixian Wang, Hannah Zhai, and Sheng Shen*

Thermal interfaces are vital for effective thermal management in modern electronics, especially in the emerging fields of flexible electronics and soft robotics that impose requirements for interface materials to be soft and flexible in addition to having high thermal performance. Here, a novel sandwich-structured thermal interface material (TIM) is developed that simultaneously possesses record-low thermal resistance and high flexibility. Frequency-domain thermoreflectance (FDTR) is employed to investigate the overall thermal performance of the sandwich structure. As the core of this sandwich, a vertically aligned copper nanowire (CuNW) array preserves its high intrinsic thermal conductivity, which is further enhanced by 60% via a thick 3D graphene (3DG) coating. The thin copper layers on the top and bottom play the critical roles in protecting the nanowires during device assembly. Through the bottom-up fabrication process, excellent contacts between the graphene-coated CuNWs and the top/bottom layer are realized, leading to minimal interfacial resistance. In total, the thermal resistance of the sandwich is determined as low as $\sim 0.23 \text{ mm}^2 \text{ K W}^{-1}$. This work investigates a new generation of flexible thermal interface materials with an ultralow thermal resistance, which therefore renders the great promise for advanced thermal management in a wide variety of electronics.

1. Introduction

The pursuit of high electronic device performance has led to a dramatic increase in processor power density, which prompts the necessity for efficient heat removal solutions.^[1–3] As a well-known thermal management bottleneck, interfacial thermal resistance between a processor chip and its heat spreader, or heat sink, is of the utmost importance for the guarantee of a reliable system.^[4,5] In addition, with the rapid development of wearable electronics and soft robotics, softness and flexibility

have emerged as indispensable properties of interfacial materials.^[6–8] Thus, there is an urgent drive toward the development of high-performance flexible thermal interface materials (TIMs) to thermally bridge the mating substrates in an effective way. An ideal TIM needs to be both thermally conductive and mechanically compliant.^[9] The former is to boost thermal transport while the latter will enable the TIM to conform to the mating surface intrinsic asperities and retain excellent contact during thermal cycling and thermal aging. As traditional TIMs can barely fulfill the two requirements at the same time, namely, solder is thermally conductive but stiff^[10] while polymer-based TIMs are compliant but hardly conductive,^[11,12] nanostructures and nanocomposites have been developed for the TIM applications. For instance, carbon nanotube arrays^[13,14] and graphene paper^[15,16] are advantageous in terms of their intrinsic high thermal conductivities, but the high contact resistance due to the dissimilar material with the joint substrate

remains problematic. Vertically aligned metal nanowire arrays, such as silver^[17] and copper nanowire (CuNW) arrays,^[18,19] are highly thermally conductive owing to their constituent material properties and are mechanically compliant attributed to the high aspect ratio of nanowires. However, in the previously reported work, they are mostly based on the direct syntheses of the nanowires from the substrate, which constrains their applicability. Oxidation is another issue for the metal nanowire arrays, which has yet to be addressed. Herein, we fabricated free-standing CuNW arrays on a $2 \mu\text{m}$ thick copper seed layer. By leveraging the 3D graphene (3DG) synthesis technology,^[20] the copper nanowires were covered by thick graphene shells which not only promote thermal performance but also achieve antioxidant. Attributed to the presence of dense hydrophobic 3DG on the CuNWs, a thin copper cap layer can be electrodeposited over 3DG-CuNWs with no copper infiltration, and consequently form excellent joints with the 3DG-CuNW tips. During device assembly, a thin tin layer can be deposited onto the top and bottom copper layers to act as the binder to join the target surfaces. In this manner, its contact resistance with the mating substrates can be substantially reduced.

Served as a TIM, it is critical to understand the thermal performance of the sandwich structure. Various methods are competent in characterizing thermal properties of thin-film structures,

L. Jing, R. Cheng, M. Tasoglu, Z. Wang, Q. Wang, H. Zhai, S. Shen
Department of Mechanical Engineering
Carnegie Mellon University
Pittsburgh, PA 15213, USA
E-mail: sshen1@cmu.edu

 The ORCID identification number(s) for the author(s) of this article can be found under <https://doi.org/10.1002/smll.202207015>.

© 2023 The Authors. Small published by Wiley-VCH GmbH. This is an open access article under the terms of the Creative Commons Attribution-NonCommercial License, which permits use, distribution and reproduction in any medium, provided the original work is properly cited and is not used for commercial purposes.

DOI: 10.1002/smll.202207015

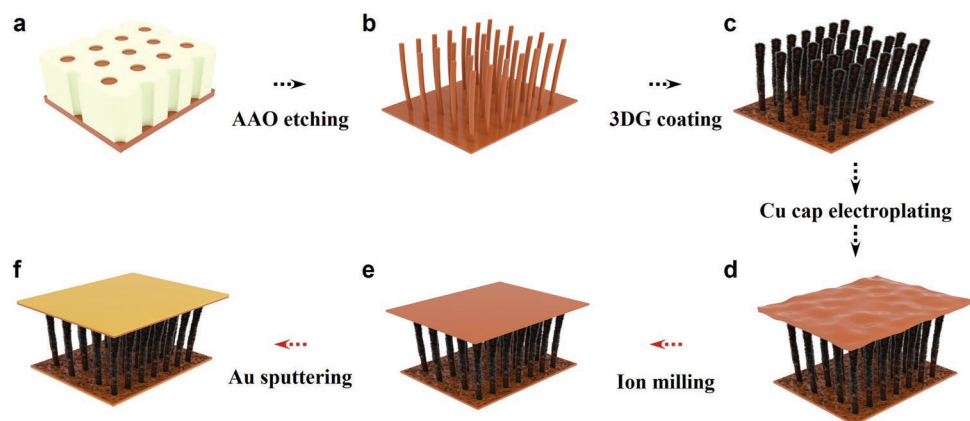


Figure 1. Fabrication of flexible sandwich TIM and specimen preparation for the FDTR measurement. a) Copper electrochemical deposition on the copper-coated AAO template. b) Free-standing vertically aligned CuNW array after wet etching. c) 3DG-CuNWs after PECVD. d) Copper-capped sandwich material. e) Ion milling process for thermal characterization. f) Gold transducer layer deposition for thermal characterization.

among which the most widely used techniques can be grouped into two categories: frequency-domain and time-domain. As an instance of the frequency-domain method, the $3-\omega$ method^[21–23] requires a microbridge fabricated on the specimen as both an electrical heater and a temperature sensor. However, as both the top and bottom copper layers of the sandwich structure are rough at the micro-level, it poses challenges to the heater fabrication. Furthermore, the requirement of an insulation layer to isolate the metal heater and the conducting sample makes sample preparation and data analysis more challenging. Therefore, contactless thermal measurement techniques are more suitable in this work. For example, time-domain thermoreflectance^[24,25] is based on pulsed pump-probe lasers, where the pump beam excites a sample while the probe beam intended for measuring the changes in the reflectivity arrives at the sample surface at different time intervals through a mechanical delay stage. Although this method has good sensitivity and is advantageous for thermal interface characterization,^[26] the complexity associated with the mechanical delay stage appears to be a major drawback.^[27] In comparison, frequency-domain thermoreflectance (FDTR),^[28–30] a similar pump-probe optical technique also based on photothermal phenomena, takes the frequency-dependent thermal response of materials as the basis, which demonstrates relative experimental simplicity. Over and above, FDTR can reliably extract thermal conductivity and interfacial conductance for a multilayer configuration. It also possesses the capability of simultaneously characterizing the in-plane and through-plane thermal conductivities, which is necessary for the anisotropic nanowire layer. Hence, we exploited FDTR to examine the thermal performance of the sandwich-structured TIM in this work. The result shows that this flexible sandwich TIM demonstrates a low intrinsic overall thermal resistance of $\sim 0.23 \text{ mm}^2 \text{ K W}^{-1}$, which is about one order of magnitude lower than conventional solders.^[10]

2. Results and Discussion

With high thermal conductivity preserved from the constituent copper and mechanical compliance realized by the high aspect

ratio, a vertically aligned copper nanowire array is leveraged as the scaffold for our TIM fabrication. The selection of nanowire dimension is a trade-off between thermal and mechanical properties. To minimize the overall thermal resistance, a short nanowire is favorable, whereas slenderness is necessary to ensure the high mechanical compliance. However, the nanowire cannot be too thin to enter the nanoscale size-dependent thermal transport regime, otherwise, the thermal benefit will be compromised. Here, we electrodeposited CuNWs of $\sim 150 \text{ nm}$ in diameter and $\sim 20 \mu\text{m}$ long using a sacrificial anodic aluminum oxide (AAO) template, prior to which a thin copper layer ($\sim 2 \mu\text{m}$) serving as the seed and support layer was sputtered on the AAO (Figure 1a). The free-standing CuNWs/Cu base structure was isolated from the AAO by wet etching and subsequent critical point drying (Figure 1b). It was then conformally coated with 3D graphene by a plasma-enhanced chemical vapor deposition (PECVD) process (Figure 1c). It is worth noting that the CuNWs possess a lower melting point than bulk copper because of the size effect. As shown in Figure 2a, CuNWs partially fused in the PECVD process at $600 \text{ }^\circ\text{C}$. Herein, a customized low temperature PECVD was employed and optimized to allow the relatively conformal and thick 3D graphene synthesis to occur at a temperature as low as $500 \text{ }^\circ\text{C}$ (Figure 2b). Raman spectroscopy (Figure 2c) was performed to examine the structure and quality of the out-of-plane graphene flakes. The representative peaks, i.e., D, G, and 2D peaks, confirm the existence of graphene. Detailed interpretation of other peaks can be referred to.^[20] In Figure 2d, the flexibility of the CuNWs/Cu base and 3DG-CuNWs/Cu base was demonstrated. The introduction of 3DG does not only bridge the heat transfer across the interface by forming additional heat paths, but also protects the CuNWs from oxidation, which would otherwise compromise the thermal performance and reliability. Moreover, the presence of the air pockets between the out-of-plane graphene flakes changes the surface from hydrophilic to hydrophobic, as shown in Figure 2e. Hence, it enables the post-electrodeposition of a thin copper cap layer on top of the 3DG-CuNW layer without copper infusion, and consequently constitutes strong joints with the 3DG-CuNW tips (Figures 1d and 2f). In this work, the final product was named as “sandwich TIM” to indicate the

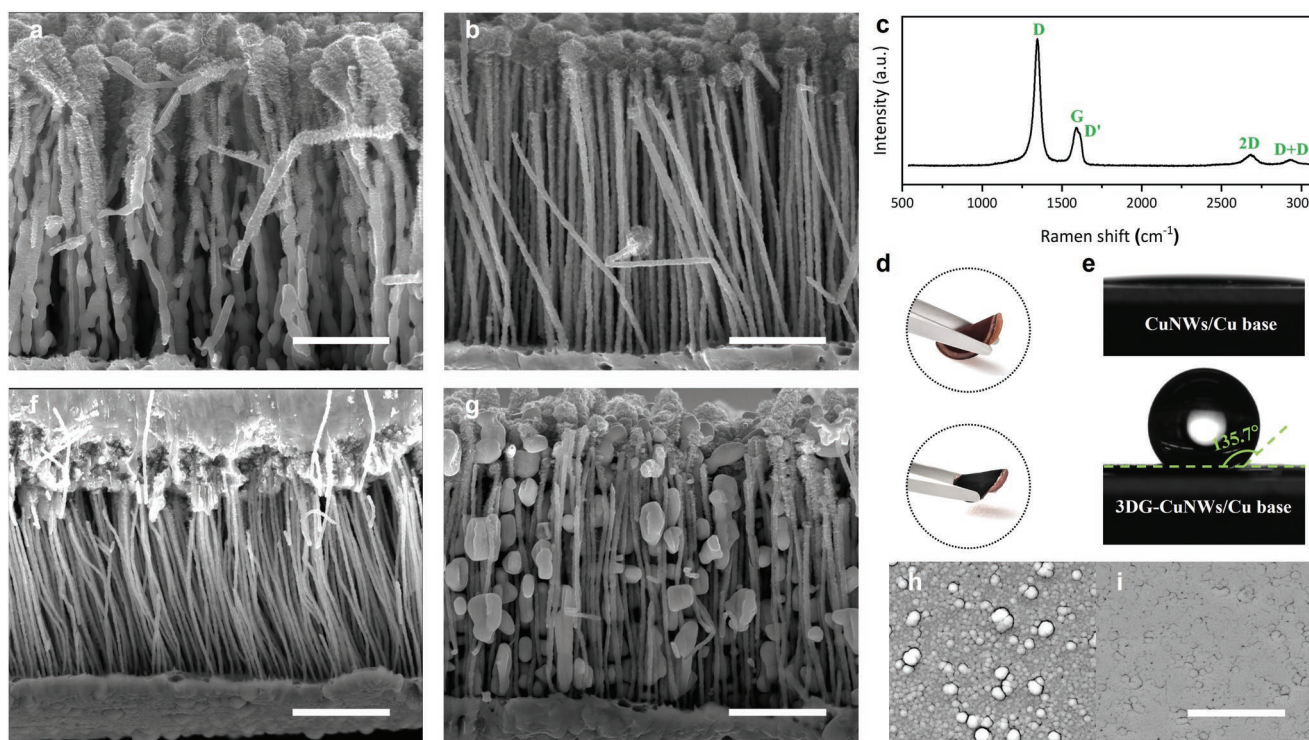


Figure 2. Sandwich TIM treatments and demonstrations. a,b) Scanning electron microscopy (SEM) of 3DG-CuNWs by PECVD at 600 and 500 °C, respectively. The CuNWs partially fuse at 600 °C, indicating the necessity of low temperature synthesis. c) Raman spectroscopy of 3DG-CuNWs. d) Optical images of CuNWs/Cu base and 3DG-CuNWs/Cu base, showing superior flexibility and robustness. e) Contact angle measurements of the CuNWs and 3DG-CuNWs. The CuNWs are superhydrophilic with a nearly 0° contact angle, while the 3DG-CuNWs are hydrophobic with a contact angle of 135.7°. f) SEM of the sandwich TIM. g) SEM of tin infiltration during electrochemical deposition without the protection of copper cap. h,i) SEM of copper base surface before and after ion milling. Scale bar in (a,b,f,g): 5 μm. Scale bar in (h,i): 10 μm.

thin copper layers laminating the vertical 3DG-CuNW array structure. In addition to transforming the contact between the material to the mating substrate from graphene-metal to metal-metal which largely reduces the contact resistance, this copper cap layer also plays a significant role in the device integration process. During device assembly, a thin tin layer (~4 μm) will be electroplated on both the cap and base sides. Sandwiched between two joint substrates, at the temperature of ~240 °C, the tin melts and flows to fill the tiny air voids. Once cooled, the mating surfaces can eventually be bonded. The existence of the copper base and copper cap can block the tin infiltration during the tin electroplating process and likewise, the bonding process, and protect the nanowires. Figure 2g shows that without the copper cap, the tin infiltrates into the CuNWs and forms solidified particles among the nanowire gaps during the electroplating. Overall, the copper cap layer is crucial to ensure device integrity. Since the flexible nanowires can readily conform to the major surface asperities, thin tin layers with only ~4 μm is required to fulfill the remaining tiny air gaps instead of the conventional ≥20 μm solder bond line thickness at the interface.

FDTR is employed to investigate the overall thermal performance of the sandwich. During the measurement, it is of great significance for the specimen to have a smooth surface. Otherwise, the scattered reflective probe signal will impact the signal-to-noise ratio and therefore the measurement accuracy. However, owing to the porous features of the AAO and

3DG-CuNWs, neither the sputtered copper base nor the electroplated copper cap is appropriately smooth for direct measurements. To address this issue, ion milling was performed on both the copper base (i.e., bottom side) and the copper cap (i.e., top side) to reveal a smooth and clean surface (Figure 1e). In Figure 2h,i, the contrast before and after the ion milling procedure on the copper base layer is exhibited. It is clearly demonstrated that surface quality is greatly improved. Lastly, a gold transducer layer of ~100 nm was sputtered on the ion-milled surface (Figure 1f) to accomplish the sample preparation for measurement.

As shown in the schematic illustration of the FDTR method in Figure 3a, the pump laser modulated over a wide frequency range (500 Hz–50 MHz) excites the sample as the heat source. Along its optical path, a matched reference detector is employed to determine the absolute phase of the pump laser that arrives at the sample surface, which is simultaneously recorded by a lock-in amplifier. The probe beam and the pump laser are directed to the same spot coaxially via a single objective lens, through which the reflectivity information carried by reflected probe beam is also led to the lock-in amplifier. The phase lag induced between a reference input from the pump laser and the reflected probe laser is collected as a function of the modulation frequency. The way to extract the unknown thermal properties is by fitting the obtained phase data to the well-known heat transfer model, which in this case is a 2D cylindrical heat conduction model for multilayer films with a Gaussian surface heat

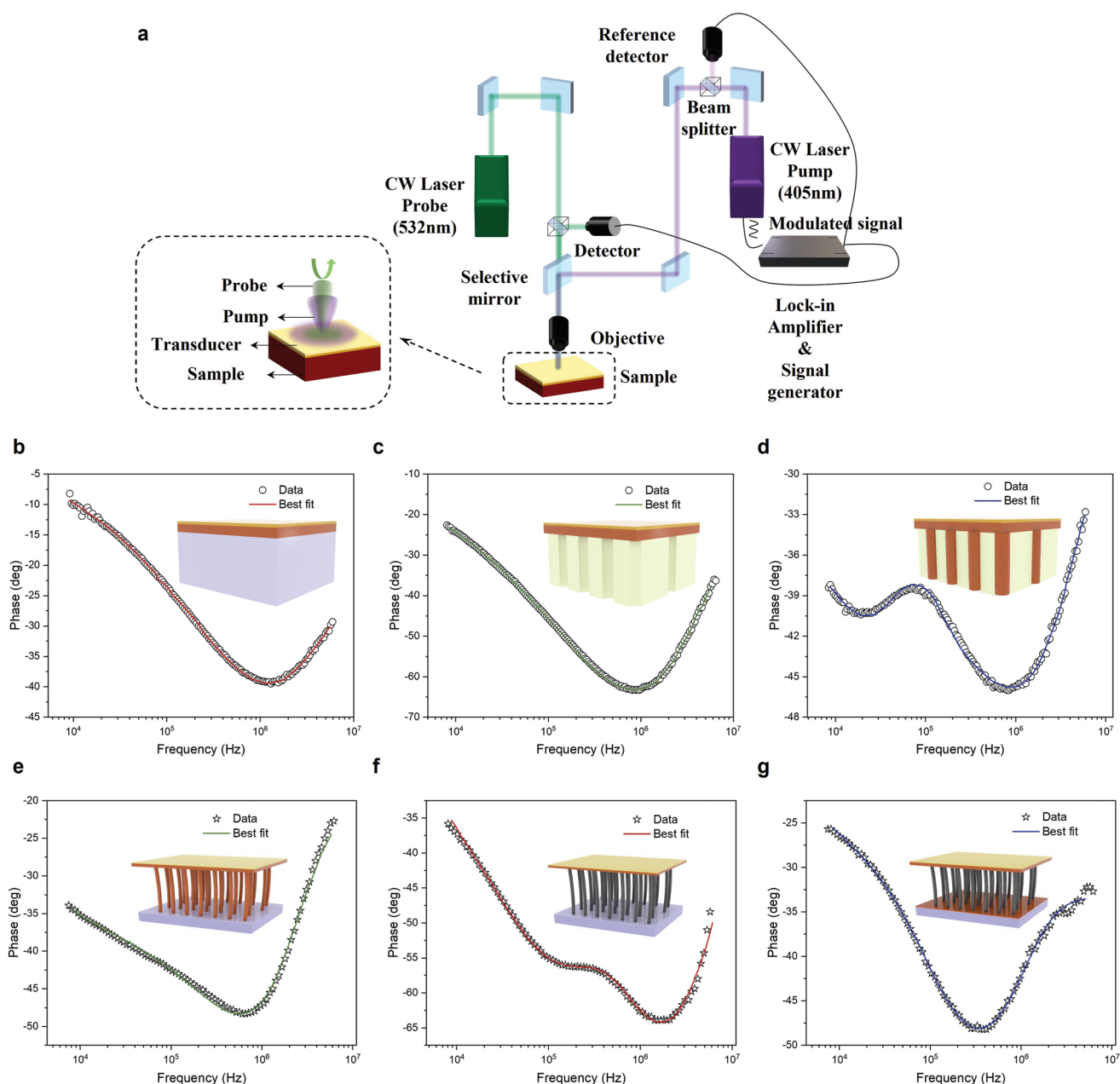


Figure 3. Experimental data and best fittings to heat transfer model in FDTR characterizations. Inset: measurement configurations. a) Schematic of FDTR measurements. b) Sputtered copper thin film. Inset: Au/Cu/Si substrate. c) Sputtered copper on AAO. Inset: Au/Cu base/AAO. d) Sputtered copper on CuNWs embedded in AAO. Inset: Au/Cu base/CuNWs-AAO. e) Free-standing CuNWs. Inset: Au/Cu base/CuNWs/insulation layer. f) Free-standing 3DG-CuNWs. Inset: Au/Cu base/3DG-CuNWs/insulation layer. g) The sandwich TIM. Inset: Au/Cu cap/3DG-CuNWs/Cu base/insulation layer.

source. Specifically, the unknown thermal properties are treated as free parameters and adjusted to find the optimal least-square fittings to the model. In this manner, the unknown thermal properties including thickness, cross-plane thermal conductivity, thermal boundary conductance, and anisotropy will be determined. As the cross-plane thermal conductivity is the main focus for a thermal interface, the thermal conductivity in the following context all refers to the cross-plane thermal conductivity. It is worth noting that an accurate transducer layer thickness has a strong effect on the data fitting. To calibrate the thickness of the transducer for every measurement, we use a silicon

substrate as a reference sample and place it next to the samples in the deposition chamber. Moreover, it is important to know the specific heat capacity c_p of the unknown layers when fitting the data. Thus, those of the CuNWs and 3DG-CuNWs were characterized by differential scanning calorimetry and the volumetric heat capacity were estimated by ρc_p , while as for the gold, copper, and AAO, their values were obtained from literature.

To progressively build the measurement confidence, the thermal characterization was achieved in the following order. First, the accuracy of the system was confirmed by measuring well-known materials, such as silicon and quartz. Next, we

measured the sputtered copper thin film thermal conductivity to verify the copper base fitting result from the subsequent sample measurements. In this step, copper with the same thickness as the copper base layer was sputtered onto a Si wafer and experienced the same ion milling procedure. In the tri-layer configuration including the transducer layer (Figure 3b), i.e., Au/Cu/Si, two boundary conductance between Au/Cu and Cu/Si, the Cu thermal conductivity, and Cu thickness served as the free parameters. Via this manner the above unknowns were determined to be $1.46e8 \pm 1.17e7 \text{ W m}^{-2} \text{ K}^{-1}$, $9.43e7 \pm 1.23e7 \text{ W m}^{-2} \text{ K}^{-1}$, $322 \pm 52 \text{ W m}^{-1} \text{ K}^{-1}$, and $1.63e-6 \pm 1.14e-7 \text{ m}$, respectively. Then the thermal properties of CuNWs embedded in the AAO template were investigated for the purpose of backing up the later free-standing CuNWs characterization. It is noteworthy that in the subsequent measurements for nano-structured specimens, including CuNWs in the AAO, free-standing CuNWs/Cu base, and 3DG-CuNWs/Cu base, the laser was incident from the copper base side (Figure 3c–f). The CuNWs embedded in the AAO sample was prepared similarly as free-standing CuNWs but without the AAO wet etching process. As an unknown in the Au/Cu base/CuNWs-AAO structure (Figure 3d), the CuNWs-AAO composite thermal conductivity appeared as $73.6 \pm 5.9 \text{ W m}^{-1} \text{ K}^{-1}$. In the same way, the measurement of a pristine AAO was supplemented to exclude the contribution from the AAO (Figure 3c). As a result, by subtracting the input of the AAO ($\sim 3.8 \pm 0.3 \text{ W m}^{-1} \text{ K}^{-1}$) which accounts for $\sim 80\%$ filling ratio, the effective thermal conductivity of the CuNWs acquired was $70.6 \pm 5.7 \text{ W m}^{-1} \text{ K}^{-1}$. Likewise, the released CuNWs were characterized by the Au/Cu base/CuNWs/insulation layer as illustrated in Figure 3e inset and was estimated to be $65.3 \pm 5.9 \text{ W m}^{-1} \text{ K}^{-1}$. The good agreement between these two scenarios within the uncertainty range further confirms the measurement reliability. Regarding the free-standing CuNWs characterization, since the thermal penetration depth ($\sqrt{2\alpha/\omega}$) (where α is the thermal diffusivity and ω is the modulated frequency in rad/s) estimated at low frequencies is comparable to the nanowire thickness, the semi-infinite substrate assumption in the thermal model is not applicable. Instead, an insulation layer was employed underneath, through which the finite nanowire layer thickness was fitted, whose accuracy was corroborated from the measurement under SEM.

Finally, with all the pre-calibrations, the Cu/3DG-CuNWs/Cu sandwich was characterized. From the perspective of measurement simplicity and fitting sensitivity, the Cu base/3DG-CuNWs and Cu cap/3DG-CuNWs boundary conductance were determined separately. To elaborate, the measurement was first done from the bottom side as the demonstrated configuration in Figure 3f inset to obtain the copper base to nanowires interfacial conductance, which was $1.23e7 \pm 9.84e5 \text{ W m}^{-2} \text{ K}^{-1}$. In this configuration, the copper base thermal conductivity and 3DG-CuNWs thermal conductivity were revealed to be 319 ± 45 and $105 \pm 14 \text{ W m}^{-1} \text{ K}^{-1}$, respectively. Similarly, due to the existence of an insulation layer below the Au/Cu base/3DG-CuNWs, the thickness of the bottom 3DG-CuNW layer was also set as an unknown and identified as $\sim 13.3 \mu\text{m}$, which was consistent with the SEM observation. Then with all other properties acquired except the copper cap conductivity k , copper cap thickness l , and its corresponding interfacial conductance G with 3DG-CuNWs, the measurement was carried out on the cap side of

the sandwich as shown in Figure 3g inset. In consequence, the outcomes were $346 \pm 48 \text{ W m}^{-1} \text{ K}^{-1}$, $5.72e-6 \pm 4.58e-7 \text{ m}$, and $9.81e8 \pm 2.26e8 \text{ W m}^{-2} \text{ K}^{-1}$, respectively. As a proof that the 3DG presence can boost the thermal performance, the 3DG-CuNWs thermal conductivity demonstrates $\sim 60\%$ improvement in comparison to CuNWs. This can be elucidated by the parallel thermal resistance model owing to the weak van der Waals interaction between the core CuNW and shell graphene flakes. Qualitatively, in the 3DG-CuNWs-air composite layer, the presence of a thick graphene layer replaces a large portion of the original air. The effective thermal conductivity of this layer is therefore composed of the contributions from copper, graphene, and air against the CuNWs, where only copper and air contribute (Equation (1)).

$$k_{\text{eff}} A_{\text{tot}} = k_{\text{Cu}} A_{\text{Cu}} + k_{\text{air}} A_{\text{air}} + k_{\text{graphene}} A_{\text{graphene}} \quad (1)$$

From the result, the obtained copper base's thermal conductivity aligns with that of the sputtered copper reference sample ($\sim 322 \text{ W m}^{-1} \text{ K}^{-1}$). The thermal boundary conductance between the thin copper layer and the nanowires on the cap side is even higher than that on the as-grown base side, which proves the excellent joint formed by electroplated copper with 3DG-CuNWs. In total, by taking account of two interfaces and three layers in the sandwich structure, the overall thermal resistance was derived by Equation (2) (where the determined thickness l of each layer was verified by SEM), which was found to be $\sim 0.23 \text{ mm}^2 \text{ K W}^{-1}$.

$$R_{\text{tot}} = \frac{l_{\text{Cu cap}}}{k_{\text{Cu cap}}} + \frac{1}{G_{\text{Cu cap/3DG-CuNWs}}} + \frac{l_{\text{3DG-CuNWs}}}{k_{\text{3DG-CuNWs}}} + \frac{1}{G_{\text{Cu base/3DG-CuNWs}}} + \frac{l_{\text{Cu base}}}{k_{\text{Cu base}}} \quad (2)$$

The sensitivity of the obtained phase signal ϕ to a parameter of interest x was quantified as follows:^[31]

$$S_x = \frac{d\phi}{d \ln x} \quad (3)$$

Properties that were extracted simultaneously from one measurement include the copper layer thermal conductivity k , despite of copper base or copper cap, thermal boundary conductance G between the copper layer and nanowires, k of nanowires, and nanowire array finite thickness. Therefore, these parameters were considered for sensitivity evaluations under the three configurations above in Figure 3e–g, while the nanowire array thickness was excluded based on the consistency between the fitted result and SEM observation. In addition, at high frequencies, the estimated thermal penetration depth in the material was much smaller than the laser spot size ($\sim 16.35 \mu\text{m}$). Hence, the measurement will approach 1D heat diffusion along the cross-plane, and only cross-plane k matters. On this account, the anisotropy of in-plane and cross-plane k in the nanowire layer can barely be a factor in the majority of the modulation frequency range and was therefore not taken into account. From Figure 4a,b, where the measurement was conducted from the copper base of CuNWs and 3DG-CuNWs, respectively, it is clear that

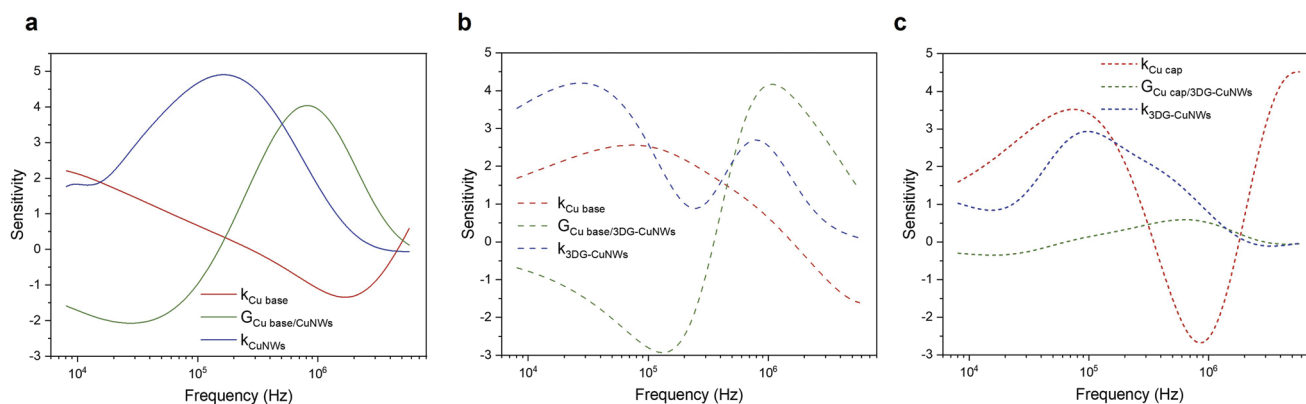


Figure 4. Sensitivity analysis. a) Copper base thermal conductivity k , copper base to CuNWs interfacial conductance G , and CuNWs thermal conductivity k configuration in Figure 3e. b) Copper base thermal conductivity k , copper base to 3DG-CuNWs interfacial conductance G , and 3DG-CuNWs thermal conductivity k configuration in Figure 3f. c) Copper cap thermal conductivity k , copper cap to 3DG-CuNWs interfacial conductance G , and 3DG-CuNWs thermal conductivity k configuration in Figure 3g.

throughout the frequency range, the sensitivities of these three parameters remained significant and distinct. Thus, it was feasible and reasonable to extract them by a single measurement. However, when the measurement was performed for the sandwich on the copper cap side as shown in Figure 4c, the sensitivity of the conductance at the Cu cap/3DG-CuNWs interface remained relatively low compared to the other two parameters. It is the relatively thick copper cap that gives rise to the low sensitivity to the boundary conductance underneath. Regardless, the interfacial conductance sensitivity varies and differs from the Cu cap k and 3DG-CuNWs k sensitivities within the frequency range and thus can be determined concurrently.

3. Conclusion

In conclusion, a flexible thermal interface material composed of a sandwich structure with a low thermal resistance was developed. FDTR was used to investigate the overall thermal performance of the sandwich TIM. As the accuracy of the measurement was validated by a thin copper film reference sample and the CuNWs in the AAO, the three layers in the sandwich and two corresponding interfacial conductance were characterized separately. The result shows that the vertically aligned CuNW array preserves its high intrinsic thermal conductivity ($65.3 \text{ W m}^{-1} \text{ K}^{-1}$). After the introduction of thick 3D graphene, its thermal performance is increased by 60% ($105 \text{ W m}^{-1} \text{ K}^{-1}$). Taking into account the extremely low interfacial resistances between the 3DG-CuNWs and the copper base as well as cap layer, the total thermal resistance of the sandwich TIM was determined to be $\sim 0.23 \text{ mm}^2 \text{ K W}^{-1}$, which is one order of magnitude lower than traditional solders. In this work, the FDTR method demonstrates great feasibility for complicated sandwich structure characterization and provides valuable implications.

Acknowledgements

This work was sponsored by National Science Foundation grant CMMI-1916110.

Conflict of Interest

The authors declare no conflict of interest.

Author Contributions

S.S., L.J., and R.C. conceived the idea and designed the experiments. L.J. and M.T. performed the sample fabrication. L.J. conducted the FDTR measurement and data analysis. L.J., R.C., and M.T. wrote the manuscript. Z.W., Q.W., and H.Z. polished the manuscript. All authors discussed the results and commented on the manuscript. S.S. supervised the research.

Data Availability Statement

The data that support the findings of this study are available from the corresponding author upon reasonable request.

Keywords

thermal interface materials, frequency-domain thermoreflectance, low thermal resistance

Received: November 11, 2022

Revised: December 25, 2022

Published online:

- [1] S. Krishnan, S. V. Garimella, G. M. Chrysler, R. V. Mahajan, *IEEE Trans. Adv. Packag.* **2007**, *30*, 462.
- [2] M. M. Waldrop, *Nature News* **2016**, *530*, 144.
- [3] T. Gebrael, J. Li, A. R. Gamboa, J. Ma, J. Schaadt, L. Horowitz, R. Pilawa-Podgurski, N. Miljkovic, *Nat. Electron.* **2022**, *5*, 394.
- [4] R. Prasher, *Proc. IEEE* **2006**, *94*, 1571.
- [5] A. Bar-Cohen, K. Martin, S. Narumanchi, *J. Electron. Packag.* **2015**, *137*, 040803.
- [6] B. D. Gates, *Science* **2009**, *323*, 1566.
- [7] K. Myny, *Nat. Electron.* **2018**, *1*, 30.
- [8] D. Shaddock, S. Weaver, I. Chasiotis, B. Shah, D. Zhong, presented at Pacific Rim Technical Conf. and Exhibition on Packaging and

- Integration of Electronic and Photonic Systems, MEMS and NEMS, ASME, Portland, Oregon, USA **2011**.
- [9] J. Hansson, T. M. J. Nilsson, L. Ye, J. Liu, *Int. Mater. Rev.* **2018**, *63*, 22.
- [10] Y. Leong, A. S. M. A. Haseeb, *Materials* **2016**, *9*, 522.
- [11] M. D. Bartlett, N. Kazem, M. J. Powell-Palm, X. Huang, W. Sun, J. A. Malen, C. Majidi, *Proc. Natl. Acad. Sci. USA* **2017**, *114*, 2143.
- [12] V. Singh, T. L. Bougher, A. Weathers, Y. Cai, K. Bi, M. T. Pettes, S. A. McMenamin, W. Lv, D. P. Resler, T. R. Gattuso, D. H. Altman, K. H. Sandhage, L. Shi, A. Henry, B. A. Cola, *Nat. Nanotechnol.* **2014**, *9*, 384.
- [13] L. Ping, P. X. Hou, C. Liu, H. M. Cheng, *APL Mater.* **2019**, *7*, 020902.
- [14] T. Tong, Y. Zhao, L. Delzeit, A. Kashani, M. Meyyappan, A. Majumdar, *IEEE Trans. Comp. Packag. Technol.* **2007**, *30*, 92.
- [15] W. Dai, L. Lv, J. Lu, H. Hou, Q. Yan, F. E. Alam, Y. Li, X. Zeng, J. Yu, Q. Wei, X. Xu, J. Wu, N. Jiang, S. Du, R. Sun, J. Xu, C. P. Wong, C. T. Lin, *ACS Nano* **2019**, *13*, 1547.
- [16] W. Dai, T. Ma, Q. Yan, J. Gao, X. Tan, L. Lv, H. Hou, Q. Wei, J. Yu, J. Wu, Y. Yao, S. Du, R. Sun, N. Jiang, Y. Wang, J. Kong, C. Wong, S. Maruyama, C. T. Lin, *ACS Nano* **2019**, *13*, 11561.
- [17] J. Xu, A. Munari, E. Dalton, A. Mathewson, K. M. Razeeb, *J. Appl. Phys.* **2009**, *106*, 124310.
- [18] M. T. Barako, S. G. Isaacson, F. Lian, E. Pop, R. H. Dauskardt, K. E. Goodson, J. Tice, *ACS Appl. Mater. Interfaces* **2017**, *9*, 42067.
- [19] W. Gong, P. Li, Y. Zhang, X. Feng, J. Major, D. DeVoto, P. Paret, C. King, S. Narumanchi, S. Shen, *Nano Lett.* **2018**, *18*, 3586.
- [20] R. Garg, S. K. Rastogi, M. Lamparski, S. C. de la Barrera, G. T. Pace, N. T. Nuhfer, B. M. Hunt, V. Meunier, T. Cohen-Karni, *ACS Nano* **2017**, *11*, 6301.
- [21] D. G. Cahill, R. O. Pohl, *Phys. Rev. B* **1987**, *35*, 4067.
- [22] C. E. Raudzisz, F. Schatz, D. Wharam, *J. Appl. Phys.* **2003**, *93*, 6050.
- [23] T. Borca-Tasciuc, A. R. Kumar, G. Chen, *Rev. Sci. Instrum.* **2001**, *72*, 2139.
- [24] R. J. Stoner, H. J. Maris, *Phys. Rev. B* **1993**, *48*, 16373.
- [25] C. A. Paddock, G. L. Eesley, *J. Appl. Phys.* **1986**, *60*, 285.
- [26] X. Qian, P. Jiang, R. Yang, *Mater. Today Phys.* **2017**, *3*, 70.
- [27] W. S. Capinski, H. J. Maris, *Rev. Sci. Instrum.* **1996**, *67*, 2720.
- [28] A. J. Schmidt, R. Cheaito, M. Chiesa, *Rev. Sci. Instrum.* **2009**, *80*, 094901.
- [29] J. A. Malen, K. Baheti, T. Tong, Y. Zhao, J. A. Hudgings, A. Majumdar, *J. Heat Transfer* **2011**, *133*, 081601.
- [30] J. Zhu, D. Tang, W. Wang, J. Liu, R. Yang, presented at *14th Intl. Heat Transfer Conf.*, ASME, Washington, DC, USA **2010**.
- [31] D. G. Cahill, *Rev. Sci. Instrum.* **2004**, *75*, 5119.